Use of sonic anemometry for the study of confined swirling flows in large industrial units

Flow Measurement and Instrumentation 50 (2016) 216–228

Contents lists available at ScienceDirect

Flow Measurement and Instrumentation

journal homepage: www.elsevier.com/locate/flowmeasinst

Use of sonic anemometry for the study of confined swirling flows in large industrial units

Víctor Francia [a,b,*], Luis Martín [b], Andrew E. Bayly [b,1], Mark J.H. Simmons [a]

[a] School of Chemical Engineering, University of Birmingham, Birmingham, UK
[b] Procter & Gamble R & D, Newcastle Innovation Centre, Newcastle upon Tyne, UK

ARTICLE INFO

Article history:
Received 29 October 2015
Received in revised form
24 May 2016
Accepted 22 June 2016
Available online 23 June 2016

Keywords:
Full scale measurement
Vortex flow
Spray dryer
Sonic anemometry
Swirl
Scale up

ABSTRACT

This work explores the methodology and errors involved in using a commercial sonic anemometer to study confined industrial swirling air flows, such as those in large cyclones or dryers in the order of hundreds of m^3. Common sources of uncertainty in time-of-flight techniques and multiple-path anemometry are evaluated and corrections and methodology guidelines are proposed to deal with issues typical of full scale measurement. In particular, this paper focuses on quantifying the error associated with the disruption of the local flow caused by a *HS* – 50 horizontal sonic anemometer under a range of turbulence characteristic of industrial swirl towers. Under the guidelines proposed and the conditions studied here, the presence of the instrument originates a measurement error <1 – 4% in velocity, <1 – 3° in direction and <7 – 31% in turbulent kinetic energy for an isothermal flow in the absence of solids. These ranges are above traditional uses of sonic anemometry in meteorology due to the limitations inherent to industrial units, but remain within reasonable margins for engineering applications. Laser diagnostic methods are widely used in laboratory and pilot scale cyclones or dryers but are rarely applicable to large production scales. In this context, the data collected with sonic anemometers render much lower resolution but appear in agreement with historical Particle Image Velocimetry. Methods such as the one proposed here can be a useful alternative to improve the level of detail of fluid dynamic studies in industrial units, which are often qualitative or with a limited validation.

1. Introduction

Laser diagnostics methods such as Particle Image Velocimetry, *PIV* [1], or Laser Doppler Anemometry, *LDA* [2–4], and the use of hot-wires [5,6] are widely applied to study swirling flows in small devices (e.g. pipes, swirlers, concentric cylinders or combustors) and larger process units such as cyclones [7–9] and dryers [10,11] in laboratory or pilot devices. On a large scale, access to these units is more complicated. The space and time available are restricted and the cost to collect data increases significantly, which makes experimentation less frequent. Lasers can provide a high spatial and time resolution but are difficult to apply in an industrial environment. Most studies are limited to scaled down devices designed *adhoc*. The application to pilot [12] or even large geometries [13] is possible but it is typically uneconomical because it carries important drawbacks: (a) disruption due to optics, (b) time and lack of flexibility due to set up and safety protocols, (c) reliability in industrial environments, (d) limited measurement range and importantly, costs associated to (e) engineering modifications, (f) time production units need to be shut down and (e) seeding. In full scale cyclones or dryers, vane anemometers [14] and flow visualization [15,16] are commonly used, but they provide a poor level of detail and cannot address many of the questions arising from models, optimization or scale up. In addition to new acoustic sensors, thermal anemometers represent a good compromise between quality and robustness [17]. Typical arrays of hot-wires are an excellent alternative for studies in a pilot scale [10,18] thanks to a high response frequency, but the set up is time consuming and too delicate for a quick and reliable use in industrial cases.

As a result of the lack of alternatives, to this date the data in large scale swirl towers or cyclones are mostly qualitative, comprised of unidirectional velocities, with no turbulence information or restricted to small sections. Consequently, scaling up the particle dynamics into the largest devices remains a challenge [19–21]. Scale-up rules arise from the experience of manufacturers, dimensional analysis of response times and the tendency of the

* Corresponding author at: School of Chemical Engineering, University of Birmingham, Birmingham, UK
E-mail address: v.francia.chemeng@gmail.com (V. Francia).
[1] Present address: School Chemical and Process Engineering, University of Leeds, Leeds, UK

http://dx.doi.org/10.1016/j.flowmeasinst.2016.06.017

Nomenclature

D	Cylinder diameter, m
G_i	The *i-th* gyration matrix
H	Distance from air inlets to vortex finder, m
R	Cylinder radius, m
Re	Reynolds number $Re = \bar{\rho}.D.\bar{U}_{av}/\mu$, -
$\bar{M}_A$	Inlet mass rate of air, kg s^{-1}
P_s	Combined path shadow $P_s = \sum_{i=1}^{i=3} s_i$
$\bar{U}_i$	Air velocity / or component in *i-th*-axis , m s^{-1}
$\bar{U}_{av}$	Bulk or superficial air velocity $\bar{U}_{av} = \bar{M}_A/\pi\rho R^2$, m s^{-1}
d	Diameter of the vortex finder, m
g	Gyration angle, °
r	Radial position, m
ra	Rotation angle, °
s_i	Shadow of the *i-th* path x 1/3
u_i	Air velocity fluctuation in the *i*-axis, m s^{-1}
x	Distance from the inner wall along D, m
y	Cartesian axis in Fig. 12, $y = 0$ for $r = 0$, m
z	Coordinate in the axial direction, m

Greek letters

Δ	Absolute error, $\Delta = \bar{X}_C - \bar{X}_E$ for variable X.
α	Misalignment, gyration over a_2, °
β	Misalignment, gyration over a_3, °
δ	Angle of attack to the horizontal plane, °
ε	Relative error, $\varepsilon = 100.(X_C/X_E - 1)$ for variable X.
γ	Misalignment, gyration over a_1, °
λ	Angle of attack to the frame axis a_2, °
κ	Specific turbulent kinetic energy, $m^2\ s^{-2}$
ρ	Density, kg m^{-3}
σ_{ij}	Variance/Covariance $u_i u_j$, $m^2\ s^{-2}$

Subscripts , superscripts and caps

1,2,3	Auxiliary axis in Fig. 5 or sonic path numbers.
a_1, a_2, a_3	Frame of reference of the anemometer in Fig. 3.
r, z, θ	Polar coordinates, along radial, vertical and tangential direction.
W', U', V'	Spar measurement axis of the HS50 Solent Anemometer in Fig. 3.
C, O	With and without the use of the internal calibration.
E	Reference estimated value.
t, b	Associated with top or bottom transducers.
*	For the door-anemometer ensemble.
$-$	Indicates time average.

powder to migrate to the walls [22]. Fluid dynamics models develop new designs and study stability [23,24], collection efficiency [25] or heat and mass transfer [26–28], but are hardly ever validated in full scale, which implies that some characteristics inherent to production are neglected, namely: (a) specific designs in industry, in particular inlet nozzles and exhaust lines (b) range of Reynolds, *Re*, and hence swirl stability and (c) comparable friction, materials or deposits. Counter-current swirl drying towers are good examples of the issues that may arise. Extensive efforts have been made to numerically describe the swirling flow [15,29,30] and compare models to data collected in laboratory [31] and pilot scale towers [12]. The attenuation of the swirl was found negligible in simplified scenarios, but *PIV* data [13] collected in production units, and later measurements with the method described here indicate that friction [32] is key to explaining how the flow and turbulence structure are generated in units with rough walls and deposits [33]. The effects of friction are beginning to be brought into modelling [34] but could only be identified after the experiments moved into full scale.

In the interest of exploring measurements in an industrial environment, this work discusses the application of a sonic anemometer to characterise the flow in large cyclones or dryers. The paper develops an alternative to study swirl flows in an array of industrial devices where lasers cannot be generally applied [17]; it provides engineers with insight to use sonic anemometers in this context and with a reasonable evaluation of some of the errors that must be expected. Guidelines to collect and correct velocity and turbulence data with a *HS50* solent sonic anemometer are given, along with a range for the measurement error under a turbulence level characteristic of industrial swirl towers.

2. Application to a large confined swirling flow

2.1. Operation of swirl tall-form dryers

This work discusses data collected in two industrial counter-current swirl dryers property of Procter & Gamble. An outline of the typical unit is given in Fig. 1a; Table 1 summarizes the design. The air enters the bottom of the unit with angular momentum due to the alignment of the inlet ports. It forms a vortex entering the cylindrical chamber and exiting through the top duct. The method proposed here allows the study of the flow in the cylindrical section where the drying droplets spend most of their residence time. The experiments were conducted under a target air mass flow rate and exit pressure, under ambient conditions and without particle production. Control loops are disabled to reduce noise.

Fig. 1b describes the velocity and turbulence profiles observed in the chamber [32]. Within the cylinder the vortex exhibits a *"concentrated"* shape [35] whereby the tangential velocity $\bar{U}_\theta$ shows a forced inner core and an outer free vortex that changes in extension as the flow moves to the top. At the central region, an axial jet (Fig. 1b2) coveys the flow towards the top exit duct. In this area, the core of the vortex precesses around the cylinder axis and the displacement results in an area of higher variability (Fig. 1b3), which indicates a periodical change in the core position rather than any real turbulent kinetic energy [32]. A more thorough description of the structure of the flow is out of the scope of this paper ; the reader is referred to other works to find more a detailed analysis of stability, structure and turbulence in a cleaned dryer [32], and how the scale and the deposits affect the structure [33]. The following sections report data sets in two spray drying towers, denoted Scale I and II in Table 1. Section 4 reports data at three radial positions in the tower Scale I. Section 5 discusses particularities of the method using data from both towers and Section 6 provides a comparison of sonic anemometry and laser based measurements.

2.2. Selection of the technique

Common techniques to study swirling flows cannot deal with the largest scales in the process industry, where one lacks fluid dynamic information to validate models and draw design and scale up criteria. As discussed before, some of the limitations arise from the use of lasers and the cost of a delicate and time consuming experimental plan. The application of sonic anemometers

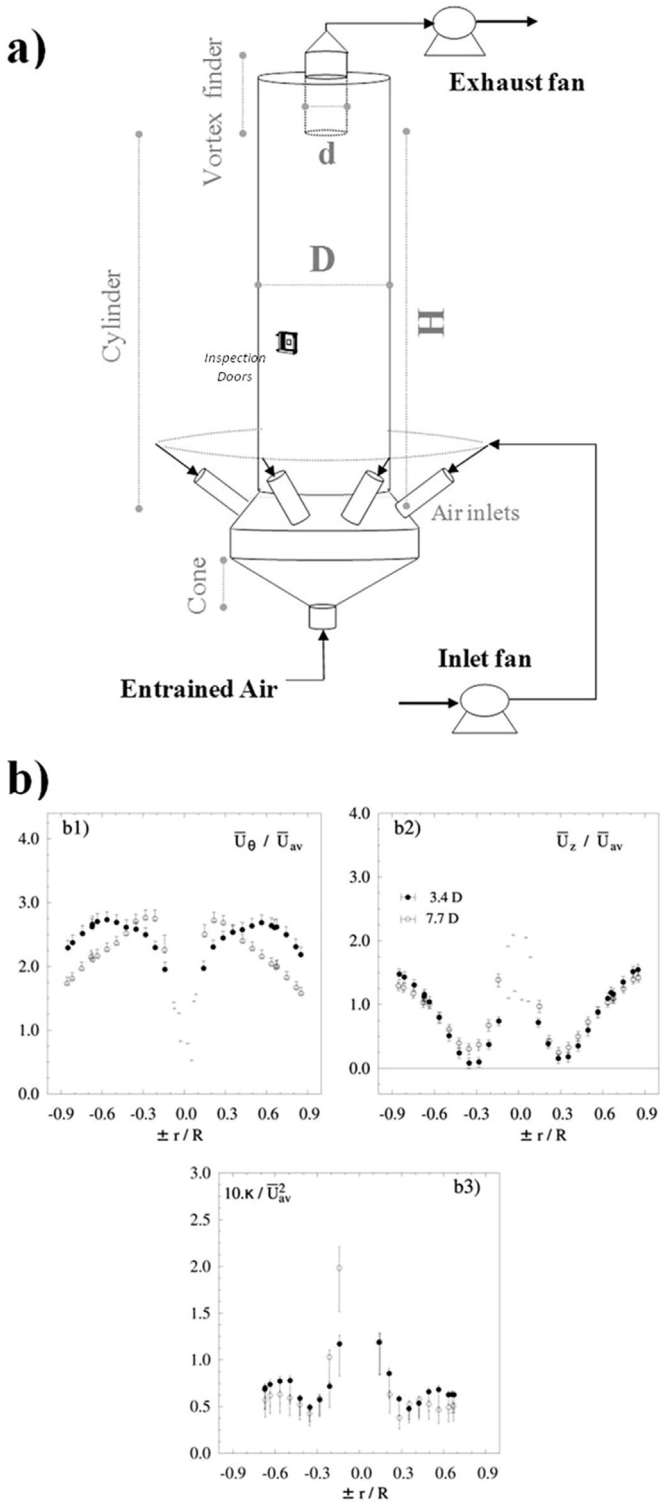

Fig. 1. (a) Outline of a tall swirl drying tower, not to scale. (b) Characteristic velocity profiles, Scale I tower, levels 3.4*D* and 7.7*D* [32] (b1) Tangential velocity $\bar{U}_\theta$ (b2) Axial velocity $\bar{U}_z$ (b3), turbulent kinetic energy κ.

can address some of the issues. Being designed for meteorological research, commercial devices are robust, handle changes in temperature and even the presence of a small amount of droplets/dust (i.e rain, snow). The instruments are easy to apply to a large confinement with affordable changes and no need for seeding. Sonic anemometers estimate the shift in the velocity of the sound

Table 1
Tower design and volume V ranges.

Design	Scale I	Scale II
$V/V_{Scale\ I}$	1.0	16.1
H/D	10.58	2.97
d/D	0.29	0.28
$Re.10^{-5}$	1.0–2.0	6.0–7.0

when it propagates in a moving medium by monitoring the time-of-flight of consecutive acoustic pulses between two or three independent pairs of transducers. Commercial research instruments provide velocity measurements in a finite sampling volume with a temporal resolution up to 50 *Hz*. Of course, the size of the instrument limits spatial resolution but considering the scale of the industrial units (e.g. $>>100m^3$) when an anemometer is applied to sufficiently large devices, the measurement volume becomes comparable to characteristic length scales of the turbulence such as in the use of finite size sensors like hot wires in smaller devices [5]. Nevertheless, accuracy is a function of the scale treated and it must be checked on a case-per-case basis contrasting sonic data with punctual measurements at high resolution. The technique itself is long established in wind engineering [36,37] to validate fluid dynamic geomorphologic models [38,39], study meteorological phenomena [40] and atmospheric turbulence [41–43], particularly the closure of the energy balance and the boundary layer [44,45]. Often, 2D devices are used to measure wind velocity, direction and fluctuation simultaneously in a set of fixed locations, but 3D instruments can also render a full spatial resolution [46]. Multi-path anemometers are common in aeronautics and eddy covariance analysis [47] for instance the estimation of axial fluxes of greenhouse gases [48–50]. Their application into industrial devices has many benefits but also some important drawbacks that need to be noticed: (a) limited spatial resolution and acquisition frequency, (b) anemometers cannot handle the process conditions in most industrial units and thus, they are limited to study the carrier phase alone in an isothermal field (c) measurement error depends on the local disruption caused by the probe and needs to be quantified in an adequate range of turbulence, and (d) care must be taken to ensure that the instrument does not disrupt the overall pressure field.

2.3. Instrumentation and methodology

A commercial research instrument *HS*–50 (Horizontal Symmetry 50 Sonic Solent Anemometer, Gill Instruments Ltd.) was selected because it is designed to minimise the drag caused by the head and transducers. The lay-out is shown in Fig. 2 along the nomenclature and frames of reference used in this paper and the definition of the angles of attack between the air and the anemometer, denoted δ and λ. Three independent pairs of transducers are mounted in a single frame with a fork-like head. The anemometer is inserted through a door that allows the movement of the instrument across the diameter of the dryer as depicted in Fig. 3a. Measurements are gathered at an acquisition frequency of 50*Hz* during 60*s* and can be taken with and without the use of an internal function that corrects the signal for the drag associated with the anemometer according to a wind tunnel calibration. Section 4 focuses in detail in quantifying the error due to the local distortion to the flow in a relevant range of turbulence for this application.

The ensemble is dismantled and moved between access points in dryers or cyclones for a period of days, weeks or months to adapt to the availability of production units (i.e. impossible with a

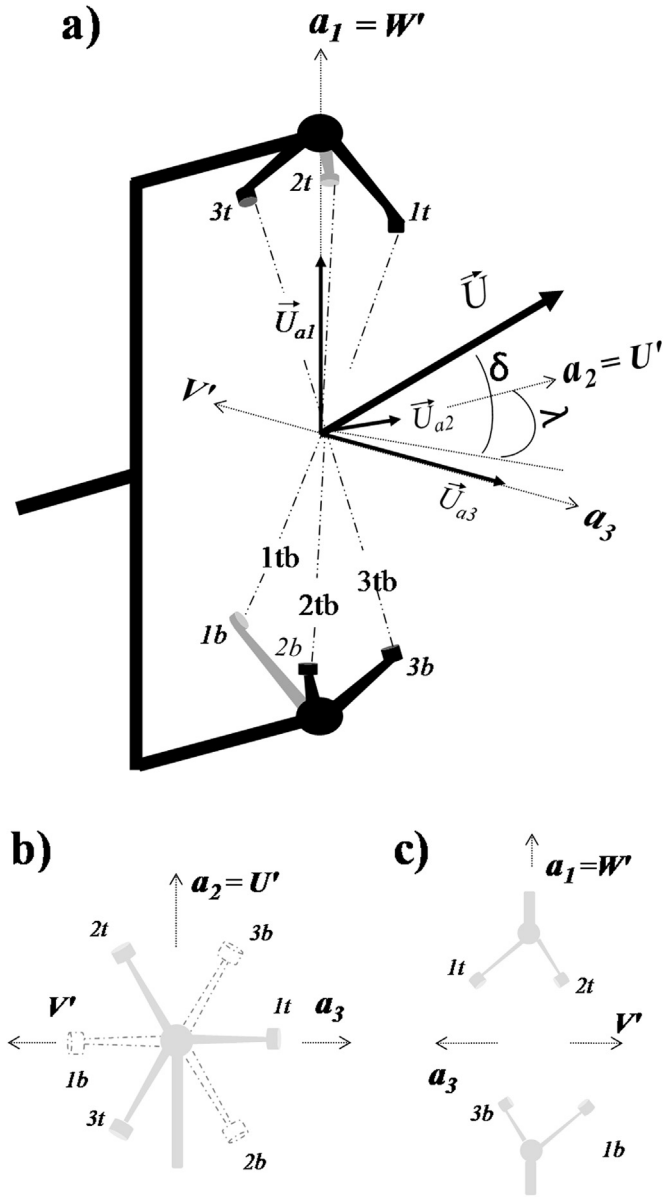

Fig. 2. Anemometer. Spar measurement axis (W', U', V') and frame of reference (a_1, a_2, a_3) for an anticlockwise air vortex (flow left to right) [51]. Angles of attack, δ, λ. (a) perspective view. (b) top and (c) front views. Not to scale.

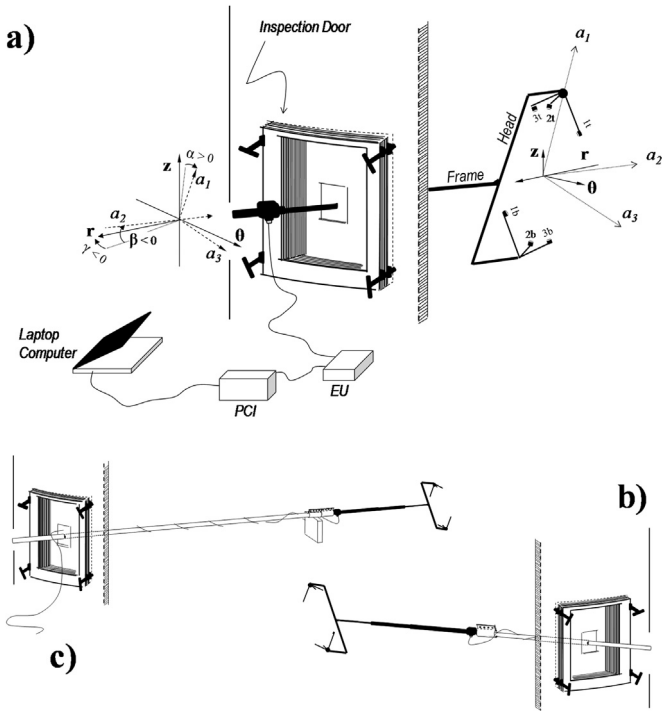

Fig. 3. (a) Ensemble, electronic unit *EU* [51] and power communication interface, *PCI* [51]. Polar frame of reference ($rz\theta$), anemometer axes (a_1, a_2, a_3) and alignments, α, β, γ [32]. (b) and (c) use of extensions. Not to scale.

more complex set up). Once the door is positioned, the frame axis a_2 is aligned perpendicular to the door. The head is positioned at a target distance from the wall x, sliding the frame in and twisting the orientation to align the axis a_1 to the cylinder vertical axis z. Fig. 3a shows the alignment left / right, denoted α, (i.e. rotation of the plane $a_1 - a_3$ over a_2) and up / down, denoted β (i.e. angle between the frame and the horizontal plane) and the alignment between the radial and the entry direction, denoted γ. The following sections detail the reasons why the target alignment is set as $\alpha = \beta = \gamma = 0$ to minimise the sources of error. During the measurement however, one must expect small deviations from this target, among other reasons because of (a) space and time restrictions (b) bending of the extension at long distances (c) alignment of the entry points and the door, and (d) misalignment of the door and the inner wall. Section 5 describes the transformations required to correct the raw signal and discuses some of the restrictions to be accounted for.

3. Issues with time-of-flight techniques

Sources of error in sonic anemometry have been widely studied in single [52] and multiple-path devices [53]. The following sections briefly discuss common issues with time-of-flight techniques, such as velocity gradients in the measurement volume or the transducer lay-out. The main source of error in sonic anemometry arises from the local disruption that the instrument itself causes in the measurement region. Errors are related to specific designs [54] and the methodology and corrections applied to the signal depending on the orientation of the anemometer [55,56]. In general terms, the distortion is minimized by an adequate selection of the instrument and the set up [57], and later corrected for by a wind tunnel calibration or other post processing algorithms [58,59].

3.1. Velocity gradients in the mean flow

Commercial anemometers emit alternate acoustic pulses of a frequency $>4.10^4 Hz$ to ensure that the wave length is much smaller than the measurement path and so apply a geometrical acoustic approach to derive the air velocity [60]. The time-of-flight principle is only strictly applicable when the air velocity across the path of the pulse is constant. In three dimensional flows, gradients and the curvature of the flow field can make the pulse deviate from a linear path and so there is a need to integrate the propagation velocity in a non-linear trajectory. The error associated to commercial instruments (i.e. assuming a linear path) has been studied for ideal flow fields and related to the velocity gradients and the field symmetry and curvature [60,61]. In general terms, errors are in the order of the second power of the Mach number. As opposed to wind engineering or aeronautics where wind speeds are very high, they pose no major concern for industrial applications (i.e. Mach $<<0.1$). In a long vortex (Fig. 1b [32]) the tangential flow is the dominant motion. In order to minimise gradients and curvature, the optimum position results from

aligning the anemometer head, a_1 with the cylinder axis z, so that axial and radial velocity gradients in the paths are minimum (i.e. order of $<0.1s^{-1}$ and $<10s^{-1}$ respectively). The exact error in this position could only be quantified if the field was known *a priori* with much higher spatial resolution (e.g. *PIV*); in this case significant errors can be discarded on the following basis: (a) the analysis in Section 4 shows that errors are limited and have an aerodynamic origin even when the gradients increase by a factor of a hundred, which should have made the error rise by several orders of magnitude if curvature was relevant [61], (b) integration of $\bar{U}_z$ across the cross-section of the dryer is in agreement with measurement of the volume rate, and (c) measurements were found in agreement with *PIV* [13] (see $\bar{U}_\theta$ in Section 6). Some regions of the chamber are excluded from this study because gradients increase significantly and the errors have not been quantified: (a) force inner vortex $r<0.10R$, (b) boundary layer $r>0.98R$ [13] and (c) vicinity of the exit $z>0.95H$.

3.2. Small angles between the sonic pulses

Relative small angles between the pulses reduce the ability to characterise three dimensional flows and lead to errors in the correction procedure of anemometers. A mathematical singularity arises at certain orientations that reduce the determinant of the Jacobian in the calibration to a null value. In essence, some directions become undefined after applying the correction to the signal, which distorts the measurement [62]. Fig. 4 illustrates this phenomenon when using a *HS*–50. The population of the angle of attack δ defined below is shown for raw and calibrated measurements in two instances that exhibit the singularity. The undefined orientation occurs only when using the calibration and in the proximity of the limit angle of attack $\delta < 45°$ given later for aerodynamic considerations, which ensures that it originates no further error in any of the measurements considered acceptable in following sections.

3.3. Shadow of transducers and supports

The presence of the anemometer causes a local disruption to the flow that depends on the relative orientation between the instrument and the mean air direction, known as the angle of attack. The orientation is defined by the angle of attack to the horizontal plane, δ, and the angle of attack to the frame axis, λ, shown in Fig. 2a and defined below:

$$\delta = cos^{-1}\left(\frac{\sqrt{\bar{U}_{a_2}^2 + \bar{U}_{a_3}^2}}{\sqrt{\bar{U}_{a_1}^2 + \bar{U}_{a_2}^2 + \bar{U}_{a_3}^2}}\right) \quad (1)$$

$$\lambda = cos^{-1}\left(\frac{\bar{U}_{a_2}^2}{\sqrt{\bar{U}_{a_2}^2 + \bar{U}_{a_3}^2}}\right) \quad (2)$$

Each anemometer is designed to operate in a range of δ and λ where errors are minimum. A wind tunnel calibration is used to correct the raw signal for the effects of the frame and the transducers as a function of the measured values of the angles of attack δ and λ. In a *HS-50*, the calibration reports an accuracy $<1\%RMS$ in velocity and 1° in direction as long as (a) $\lambda>30°$, which ensures the frame and the head do not block the flow (see Fig. 2a) and (b) $\delta<50°$, which ensures that the transducers themselves do not block the measurement region (see Fig. 2a).

The level of turbulence in wind/air flows also has important effects on the error [63,64]. As fluctuations increase, the air attacks the instrument across a wider range of direction (δ and λ), which cannot be described properly by using average values to calibrate

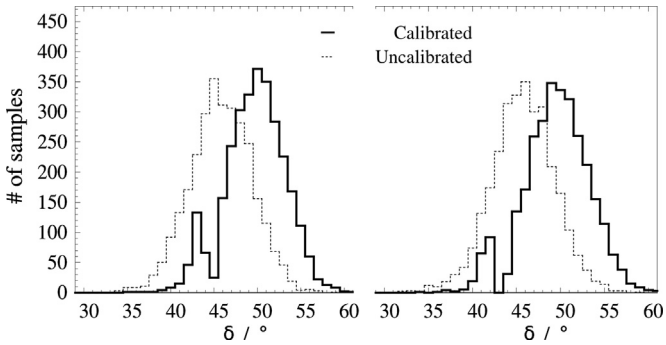

Fig. 4. Examples of singular orientations in the angle of attack δ.

the instrument or to set the limit angles of attack to consider measurements acceptable. In a traditional meteorological application the instrument would be realigned to the mean wind direction in order to minimise δ close to 0° and maximise λ close to 180°. In this manner, most of the fluctuations from the average direction remain within the limit angles and the disruption is minimal. Measurements in a confined unit are necessarily different. The level of turbulence is higher and so the error must be studied independently. Besides, it is impossible to realign the anemometer to an optimum orientation every time because it would imply enormous costs in terms of time and engineering entry points. Instead, this work proposes to keep the anemometer at a constant orientation versus the cylinder (i.e. a_1 aligned with z thus $\alpha = 0$, and a_2 aligned with r thus $\beta = \gamma = 0$), which optimises the values of the angles of attack (δ, λ) when the flow is tangential (δ=0° , λ=90°). Indeed, cyclones or dryers exhibit a strong swirling flow where the tangential motion is dominant, but in general, also present smaller axial and radial velocities. In this way, when the anemometer is placed at different locations in the flow field (moved from one to another place in the dryer), the angles of attack (δ, λ) become a function of the air direction in that specific point. Using the orientation proposed here to study a large long vortex results in angles of attack below the limits for the most part of the chamber, and therefore the measurements are adequate. Only in sections where the axial flow ($U_{a_1} = U_z$) dominates the motion δ rises >50° and the measurements must be discarded (e.g. core in Fig. 1b). The horizontal angle of attack λ is less restrictive because with the exception of the core and the exit duct, the radial velocity is very low and λ~90°. Of course, lower spatial resolution, stronger turbulence and angles of attack that are in general above the optimum make errors higher than in typical uses of sonic anemometer such as the research of atmospheric turbulence. However, considering the lack of alternatives in this type of units, the data can easily accept higher errors and remain valuable.

4. Quantification of the local flow disruption in a large turbulent vortex

Wind tunnel calibrations are carried out under near laminar conditions and cannot be *a priori* considered representative of such industrial applications where turbulence must be accounted for [63,64]. This section quantifies the measurement error in this application as function of the angle of attack δ and under a range of turbulence characteristic of a swirl dryer. It studies how the velocity signal changes when the anemometer is revolved at a fix point. The instrument was placed at three radial positions in the tower Scale I where the flow is mainly tangential, and the head was rotated (see Fig. 5) in such a way that the transducers are

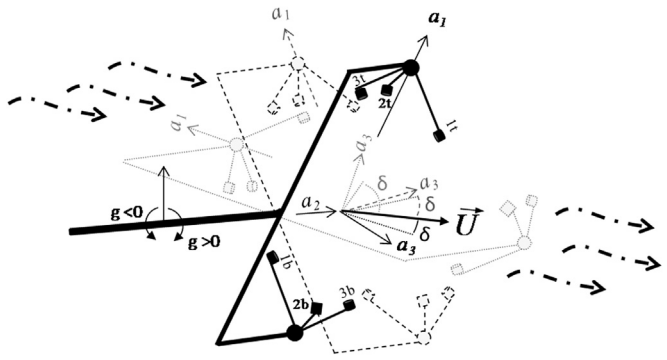

Fig. 5. Revolution of the anemometer facing a tangential flow.

progressively aligned against the flow (i.e. U_{a_1} and δ increase while the velocity and turbulence remain constant). The analysis has been repeated at positions that cover the range of turbulence kinetic energy from $\kappa/\bar{U}_E^2$ =0.005 to 0.026 (data available in Supplementary material).

Fig. 6 illustrates the revolution. Initially, the head frame a_1 is aligned with the vertical axis of the tower, z, and the velocity components in polar coordinates ($U_r U_z U_\theta$) are equivalent to those in the anemometer frame of reference ($U_{a_1} U_{a_2} U_{a_3}$) defined in Figs. 2 and 3. The head then rotates over a_2 and measurements are taken in calibrated and un-calibrated mode at 50 gyration angles, denoted g (g>0° clockwise and g<0° anticlockwise; note that $g = \alpha$, this notation is used here to distinguish the error analysis from the standard methodology). As the head revolves a_2 remains aligned with the radial direction r and only a_1 and a_3 change. It is important noticing that due the way the transducers are layout in a *HS*–50, the position obtained for g in clockwise or anticlockwise sense differs (e.g. compare g=60° and g = – 60° in Fig. 6). The same geometry is obtained for rotation angles *ra* such that *ra* = g in clockwise direction and *ra* = g+180° in anti-clockwise direction (e.g. compare g=60° and g = – 120° in Fig. 6). Table 2 defines the two equivalent sets of positions resulting from one revolution, Sets A and B. Fig. 6 illustrates the position for each rotation angle *ra* in Set A, where g>0° (moving from left to right with the bottom transducers upstream) and Set B, where g<0°(moving from right to left with the top transducers upstream).

Table 2
Equivalent positions in the revolution.

Design	Set A	Set B
Gyration angle, g	0<g < 180	−180<g < 0
Rotation angle, ra	ra = g	ra = g + 180
Upstream transducers	bottom	top

The response of the measurement when the head revolves is described in Fig. 7. The real values are given by the best estimate of velocity, direction and turbulence statistics, denoted by an E subscript and obtained from the average of measurements where δ < 5°. The variation expected for each variable during the revolution is denoted by a solid line and computed according to the change in coordinates. The actual measurements are recorded with or without the calibration and denoted with open and solid markers and O or C subscripts respectively. Fig. 7 shows how the measurements start to deviate significantly from the expected values when the angles of attack increase above a certain limit. The revolution commences at $g = 0°$ where the disruption is negligible (see δ~0° in Fig. 7c, where δ_{90th} denotes the 90^{th} percentile of δ). As the head revolves, the frame and the transducers start to disrupt the flow and the angle of attack increases. As a result of the drag the measurement of the velocity starts to exhibit a deficit error between the estimated and measured values, $\bar{U}_C - \bar{U}_E$ (i.e. Fig. 7a). The change in coordinates makes the velocity in the axial and tangential direction $\bar{U}_{a_1}$ and $\bar{U}_{a_3}$ to be swapped during the revolution (Fig. 7e and f). The axial flow (i.e. $\bar{U}_{a_1}$) is the most susceptible to drag in this anemometer and thus it shows the highest measurement bias, −20% at the largest value of the angle of attack, δ_{90th}, when the transducers block the flow. In addition, the mean direction, λ (i.e. Fig. 7b), becomes strongly distorted

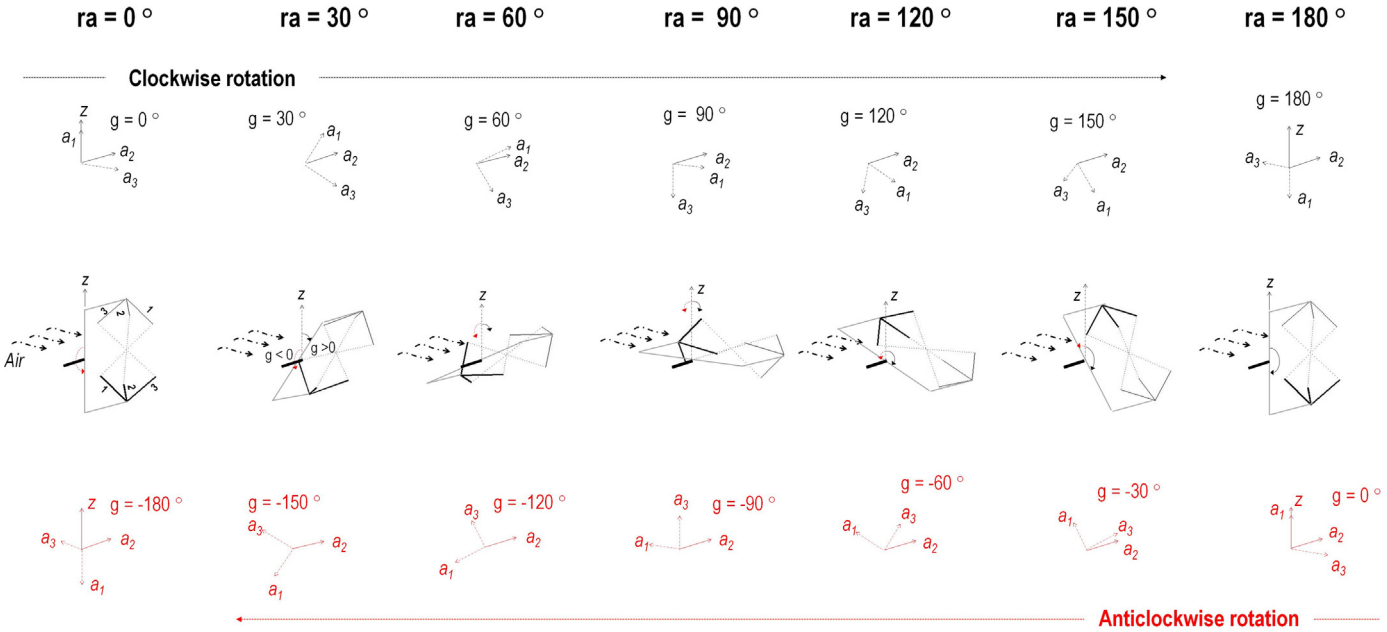

Fig. 6. Orientation of the head and the transducers during the revolution. Position and anemometer frame of reference in a clockwise rotation (moving from left to right Set A, Table 2) and an anticlockwise rotation (moving from right to left Set B , Table 2). The set of transducers upstream is responsible of the drag and given in bold: it corresponds to the bottom in Set A or the top in Set B.

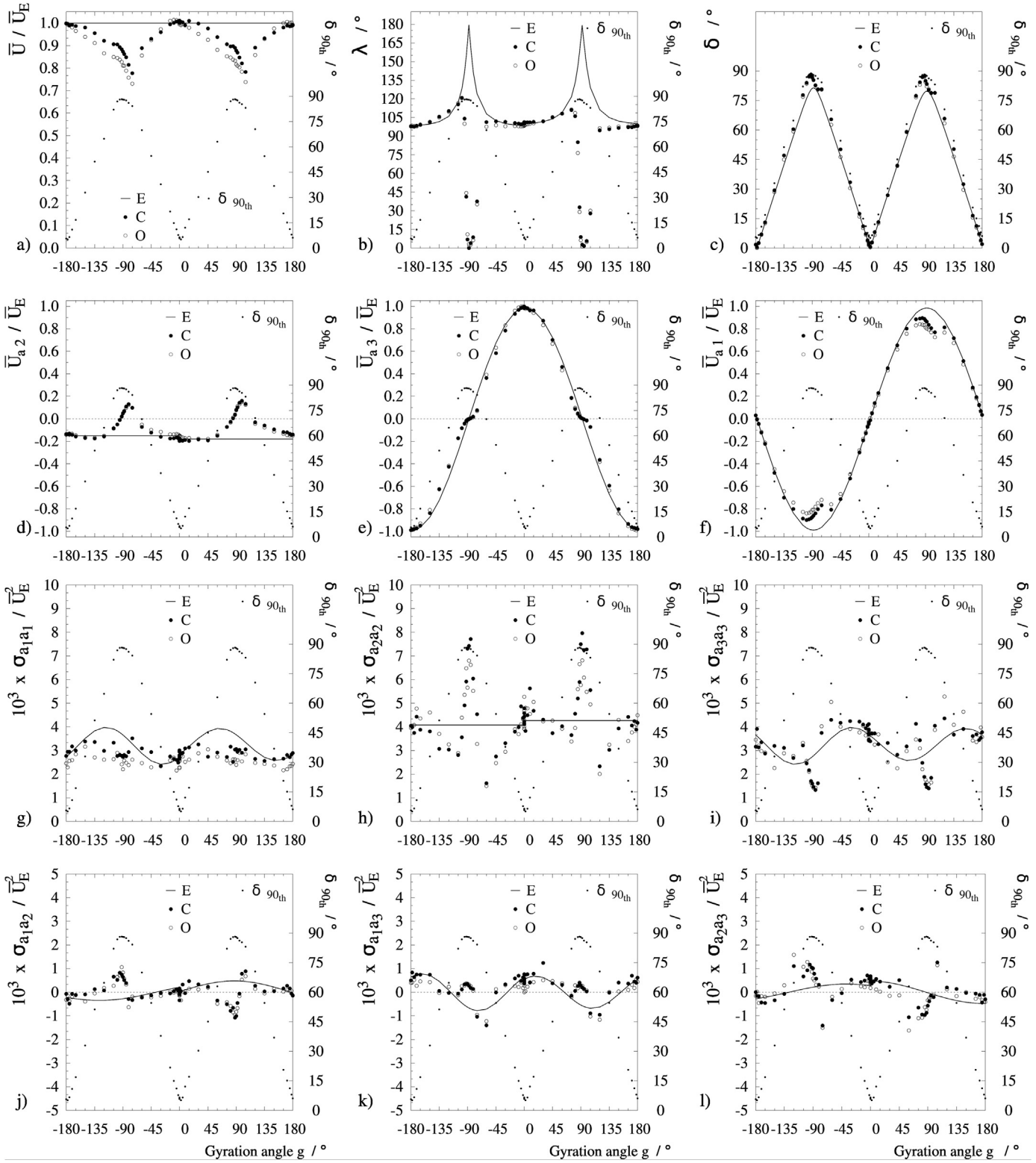

Fig. 7. Evolution of the error in the measurement of velocity and turbulence during the revolution in the anemometer frame of reference ($a_1a_2a_3$). Data for Scale I tower, r=0. 35R, $\kappa/\bar{U}_E^2$ =0. 005. (a) $\bar{U}$ (b) λ (c) δ (d) $\bar{U}_{a_2}$ (e) $\bar{U}_{a_3}$ (f) $\bar{U}_{a_1}$ (g) $\sigma_{a_1a_1}$ (h) $\sigma_{a_2a_2}$ (i) $\sigma_{a_3a_3}$ (j) $\sigma_{a_1a_2}$ (k) $\sigma_{a_1a_3}$(l)$\sigma_{a_2a_3}$. E, C and O denote respectively estimate, calibrated and non-calibrated measurements.

when the angle of attack δ_{90th} moves >45°. Above this point, the drag originates a clear perturbation in the radial flow, $\bar{U}_{a_2,C} - \bar{U}_{a_2,E}$ that changes sense (i.e. Fig. 7d). Fig. 7g to l include the deviation of the turbulence statistics. The perturbation observed in the radial flow in Fig. 7b and d translates here into artificial measurement of turbulence at the positions associated to the strongest drag (i.e. δ_{90th}>45°), which becomes particularly visible in the radial normal stress σ_{a_2,a_2} (Fig. 7h).

In Fig. 7, the profiles are not symmetrical about g~0°, but maximum errors are reached at g~−75° and g~105°. This is a 3D

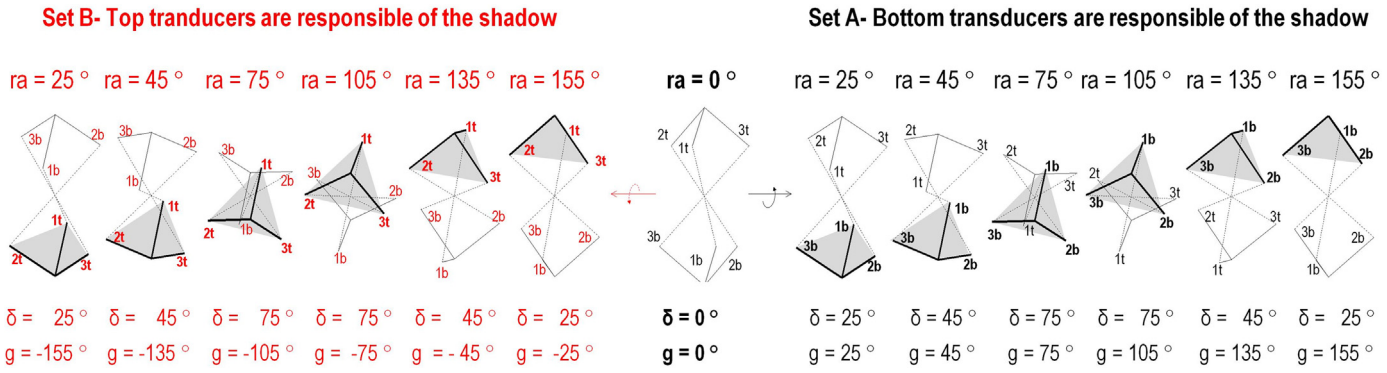

Fig. 8. Disrupted volume. Projection of along the streamline (the flow moves into the page) as function of δ for λ=105°. Grey areas delimit the shadow cast by the surface comprised of the transducers upstream.

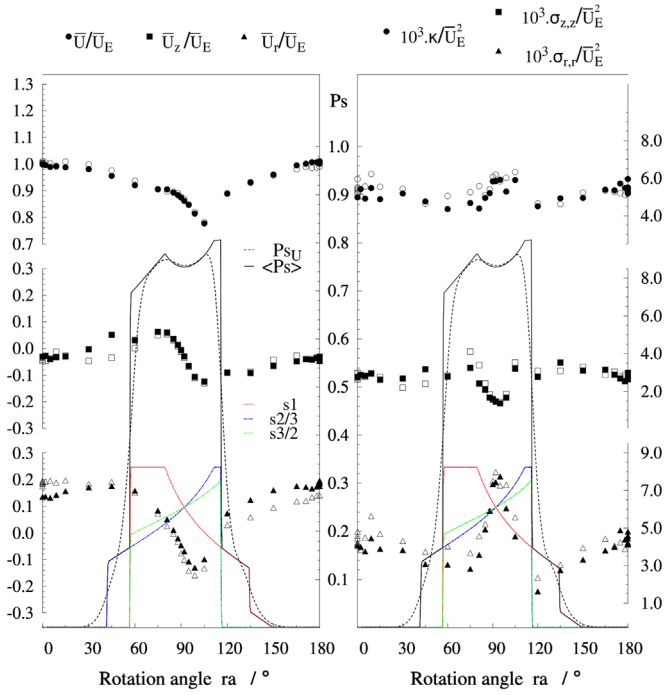

Fig. 9. Correlation of error to path shadow. Calibrated mode, Scale I tower, r=0. 35R, $\kappa/\bar{U}_E^2$=0. 005, filled and open symbols denote Set A and B in Table 2. Velocities $\bar{U}_r$ and $\bar{U}_z$ (left axes) and normal stresses $\sigma_{r,r}$ $\sigma_{z,z}$ (right axes). The path shadow Ps (central axis) gives the ratio of the paths included in the volume disrupted (Fig. 8). Ps_U gives the shadow cast by the mean air direction and $\langle Ps\rangle$ the time-averaged shadow. s_i denotes the contribution of each path to Ps_U (see nomenclature).

effect that cannot be described with the usual definition of δ given in Eq. (1) between 0 and 90° but can be explained by considering the shadow cast by the transducers. Each transducer disrupts the field downstream, but it is the orientation what determines whether the local perturbation affects the measurement volume. Fig. 8 shows the projection of the transducers head along the air streamline as function of g and δ in a purely tangential flow. As the head revolves the shadow cast by the transducers is projected into the path of the sonic pulses, which causes the increase in error. Notice that positions with the same δ can in fact produce different drag areas (e.g. see how δ=75° may result from two layouts where either one transducer, `1´, or two , `2´ & `3´, are responsible for the drag depending on whether the bottom or top transducers are upstream in Sets A or B). Fig. 9 presents the correlation between the shadow cast by the transducers and the error pattern. The two set of positions that share the same geometry in Fig. 6 and Table 2 show overlapping trends in Fig. 9. The regions at either side of ra=90° correspond to the positions where the transducer 1 blocks the sonic path 1tb or the transducers 2 – 3 block the paths 2tb and 3tb (see δ=75° in Fig. 8 and the corresponding individual path shadows in Fig. 9). Interestingly, both sides of ra=90° show clearly different profiles and it is precisely the transition between them which originates the change in sense of the radial flow and the large perturbation observed in the variability (Fig. 9). Data extended to the other positions and normal and Reynolds stresses are given in Supplementary material. The fact that this asymmetry exists and that the error pattern can be linked to the shadows, exclusive function of geometry, is relevant. It shows the aerodynamic origin of the error and confirms that it is not purely determined by δ but also by the sense of U_{a_3}, in an indication that δ may be better defined from 0 – 180°.

Fig. 10 shows the resulting distribution of error in the velocity magnitude, direction, and turbulence as a function of δ_{90th} for the measurements during the revolution. Table 3 presents the maximum error range for the measurements that comply with the limits δ_{90th}<45° and λ_{90th}>30°. These ranges are characteristic of the turbulence in an industrial tower and cover the full range of possible angles of attack when one moves the instrument from one to another location. Thus, they may be consider a conservative estimate of the error when one collects data with a HS–50 at any position as long as the flow exhibits a similar structure and the same limit angles and guidelines are considered.

5. Methodology guidelines in full scale

5.1. Time averaging

The measurement time needs to be sufficiently high to ensure the convergence of the statistics with sufficient accuracy. It is particularly true in cyclonic flows that tend to exhibit variability in large time scales as well as oscillations and periodical flows [23,24,65]. It is equally true that the costs of working with a production unit make impossible to collect data for very long periods of time. Indeed, costs explain the lack of data and one must try reducing the measurement time as much as possible while keeping the data meaningful. Any limitation however makes studying the largest time scales in the flow impossible and introduces an error, but in practise, it is essential to access production units. In an oscillating swirling flow the minimum time would depend on the design and scale of the unit and thus it must be checked on a case-per-case basis. In this work, the error arising from reducing the averaging time was checked in several positions. Fig. 11 illustrates how a certain large time scale variability

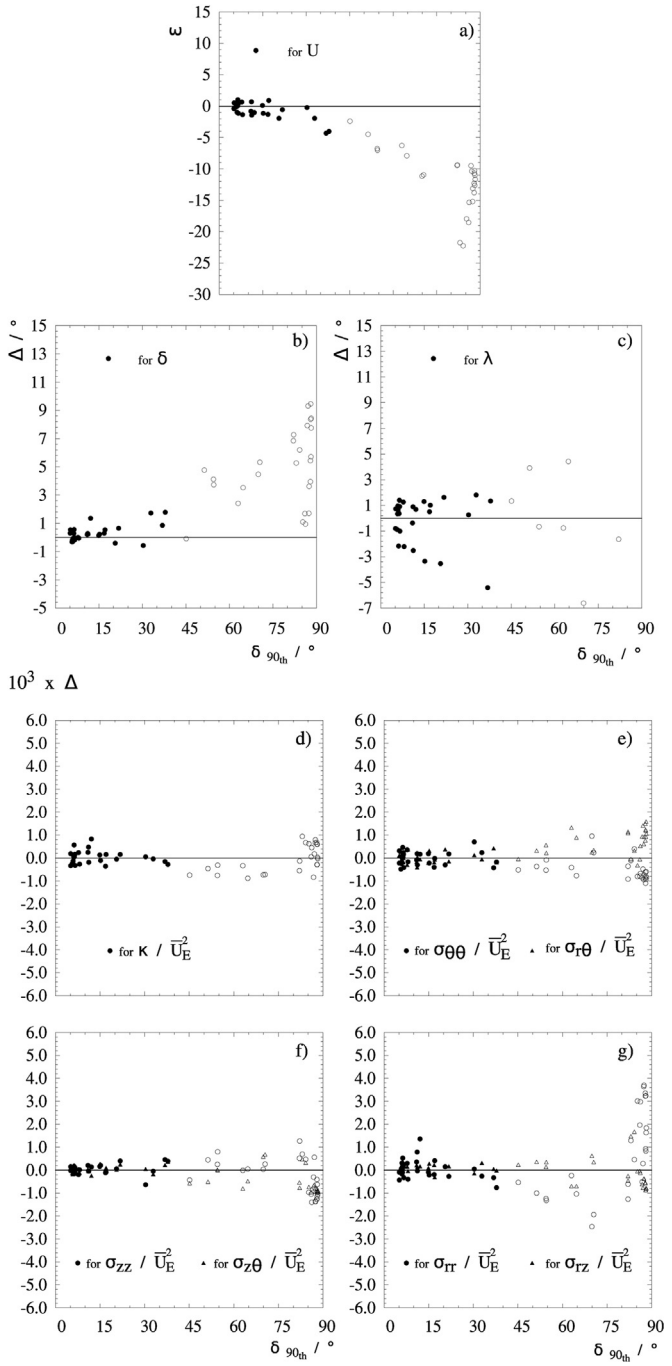

Fig. 10. Errors as a function of the 90th percentile of the angle of attack $\delta_{90_{th}}$. Scale I tower, r=0. 35R, $\kappa/\overline{U}_E^2$=0. 005. Calibrated mode. The solid symbols indicate the data complying with $\lambda_{90_{th}}$>30° , $\delta_{90_{th}}$ < 45°, Absolute Δ or relative error ε for (a) $\overline{U}$ (b) δ (c) λ (d) κ (e) $\sigma_{\theta,\theta}$, $\sigma_{r,\theta}$ (f) $\sigma_{z,z}$, $\sigma_{z,\theta}$ (g) $\sigma_{r,r}$,$\sigma_{r,z}$.

Table 3
Range for the measurement error in the revolution when the direction complies with the limit angle of attack δ_{90th}<45°, λ_{90th}>30° under calibrated mode. Absolute Δ and relative error ε (see nomenclature).

Variable X	X_E	Δ *or* ε		
	average	*range*	*min*	*max*
r=0.35R				
δ	2.4°	2.4°	−0.6°	1.8°
λ	99.5°	7.2°	−5.4°	1.8°
$\overline{U}$	$\overline{U}_E$	5.3%	−4.3%	1.0%
$\kappa/\overline{U}_E^2.10^3$	5.3	22.3%	−6.7%	15.6%
$\overline{u_z u_z}/\overline{U}_E^2.10^3$	4.2	50.6%	−18.7%	32.4%
$\overline{u_\theta u_\theta}/\overline{U}_E^2.10^3$	3.6	32.6%	−13.4%	19.3%
$\overline{u_r u_r}/\overline{U}_E^2.10^3$	2.7	39.5%	−22.4%	16.5%
r = 0.60R				
δ	12.3°	3.0°	−1.4°	1.6°
λ	95.8°	3.9°	−2.8°	1.1°
$\overline{U}$	$\overline{U}_E$	3.3%	−3.0%	0.4%
$\kappa/\overline{U}_E^2.10^3$	7.8	37.5%	−6.2%	31.3%
$\overline{u_z u_z}/\overline{U}_E^2.10^3$	5.9	57.5%	−16.5%	41.0%
$\overline{u_\theta u_\theta}/\overline{U}_E^2.10^3$	4.2	42.6%	−19.4%	23.1%
$\overline{u_r u_r}/\overline{U}_E^2.10^3$	5.5	42.1%	−6.7%	35.3%
r = 0.10R				
δ	25.9°	8.1°	−1.5°	6.6°
λ	108.0°	7.5°	−3.0°	4.5°
$\overline{U}$	$\overline{U}_E$	19.1%	−14.5%	4.6%
$\kappa/\overline{U}_E^2.10^3$	26.5	31.3%	−17.7%	13.6%
$\overline{u_z u_z}/\overline{U}_E^2.10^3$	21.9	35.0%	−18.9%	16.1%
$\overline{u_\theta u_\theta}/\overline{U}_E^2.10^3$	17.1	71.0 %	−31.5%	39.4%
$\overline{u_r u_r}/\overline{U}_E^2.10^3$	13.9	34.7%	−15.5%	19.3%

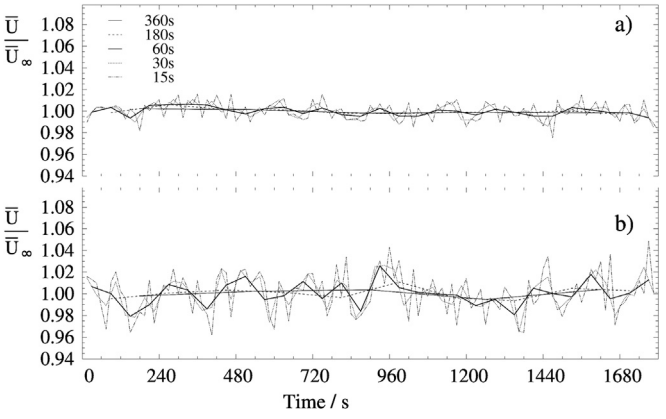

Fig. 11. Average air velocity for decreasing averaging times.

appears for averaging times <360*s*. In this case study, a measurement time of 60*s* was considered a good compromise to limit error and preserve the flexibility of the method. It allowed large geometries to be covered and it was sufficient to reduce the variability in the time-averaged velocity (<1% and <2% in Fig. 11a and b for $\kappa/\overline{U}_E^2$ = 0.008 and 0.035) and the turbulence statistics below the errors expected from the local disruption.

5.2. Correction for the actual anemometer orientation

After positioning the anemometer, the actual alignments α and β are measured by an in-built inclinometer. In a large scale unit, it is vital to account for deviations from the target orientation. In particular, one must consider the adjustment of the mechanical fittings, see Fig. 3a, because the doors are often misaligned with the walls. A deviation between a_2 and the radial direction, r, denoted γ, can lead to very large errors in U_θ and U_r. The transformations outlined below express the raw signal in polar coordinates. The position of measurement is related in Eq. (6) to the position and alignment of the ensemble shown in Fig. 3. The latter can be estimated by manually measuring the offset between the radial direction r and the projection of the orthogonal to the door in the plane $r-\theta$, denoted Δ_y and depicted in Fig. 12. The

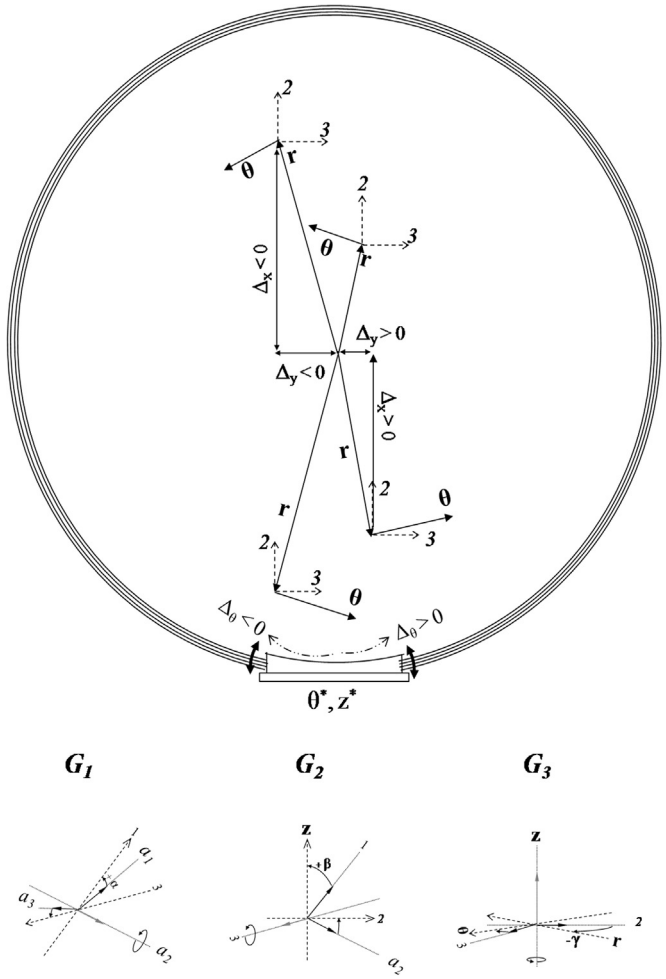

Fig. 12. Position and misalignment of the ensemble in the horizontal plane.

subsequent offsets in x and θ are denoted Δ_x and Δ_θ and computed in Eqs. (3) and (4).

$$\Delta_x = \sqrt{R^2 - \Delta_y^2} - x^*.\, cos\beta \tag{3}$$

$$\Delta_\theta = sin^{-1}\left(\frac{\Delta_y}{r}\right) \tag{4}$$

Whenever $\Delta_y \neq 0$, a gyration angle γ is required to align the auxiliary axes 2 and 3 in Fig. 12 with the true r and θ. Depending upon the relative position of the anemometer versus the centre-line, γ reads

$$\gamma = \begin{cases} \Delta_\theta & for \quad \Delta_x > 0 \\ \pi - \Delta_\theta & for \quad \Delta_x < 0 \end{cases} \tag{5}$$

The position in cylindrical coordinates r, z, θ is expressed in Eq. (6) as function of the position of the door θ^* and $z^*$and the distance of the head into the cylinder x^*.

$$\begin{bmatrix} r \\ z \\ \theta \end{bmatrix} = \begin{bmatrix} \sqrt{\Delta_x^2 + \Delta_y^2} \\ z^* + x^*.\, sin\beta \\ \theta^* + \gamma \end{bmatrix} \tag{6}$$

The following transformations can be used to express the velocity data measured along the spar axes W', U', V' and the reference axes a_1, a_2, a_3 into the polar frame of the cylinder, denoted r, z, θ.

$$\begin{bmatrix} u_{a_1} \\ u_{a_2} \\ u_{a_3} \end{bmatrix} = \begin{bmatrix} W' & U' & V' \end{bmatrix}.\, G_0 \tag{7}$$

$$\begin{bmatrix} u_z \\ u_r \\ u_\theta \end{bmatrix} = \begin{bmatrix} u_{a_1} & u_{a_2} & u_{a_3} \end{bmatrix}.\, G_1.\, G_2.\, G_3 \tag{8}$$

where G_i are functions of the instrument alignment:

$$G_0 = \begin{bmatrix} 1 & 0 & 0 \\ 0 & 1 & 0 \\ 0 & 0 & S \end{bmatrix} \tag{9}$$

$$G_1 = \begin{bmatrix} cos\alpha & 0 & sin\alpha \\ 0 & 1 & 0 \\ -sin\alpha & 0 & cos\alpha \end{bmatrix} \tag{10}$$

$$G_2 = \begin{bmatrix} cos\beta & -sin\beta & 0 \\ sin\beta & cos\beta & 0 \\ 0 & 0 & 1 \end{bmatrix} \tag{11}$$

$$G_3 = \begin{bmatrix} 1 & 0 & 0 \\ 0 & -cos\gamma & sin\gamma \\ 0 & sin\gamma & cos\gamma \end{bmatrix} \tag{12}$$

G_0 sets the reference axes in the raw signal in Eq. (7) and sets the positive direction of a_3 with the sense of rotation of the flow, where S reads -1 or 1 for an anticlockwise or clockwise vortex. The first and second terms in Eq. (8) account for the alignment of the head with a first gyration over the frame axis a_2 in G_1, and a second in G_2 over the perpendicular to the anemometer plane (axis 3 in Fig. 12). In this manner, one axis aligns with z while the remaining (2 and 3) are contained in the horizontal plane $r - \theta$. The third term G_3 accounts for the door. A gyration over z aligns both axes in the horizontal plane with r and θ, setting a positive sense in the radial direction outwards.

5.3. Disruption of the development of the vortex

Swirling flows oscillate and can be easily distorted. Given this method is intrusive in nature, one must ensure that the presence of the instrument does not affect the overall development of the pressure field, which is an obvious assumption in meteorology or natural swirling flows, but not in a confinement. It has been noticed that the presence of the anemometer in the central region (i.e. jet-like region in Fig. 1) distorts the turbulence field. Fig. 13 shows examples where an extension was used to collect data (see Fig. 3b). Measurements taken when the anemometer reaches a position without crossing the centre are denoted with solid symbols (the anemometer penetrates a length $x < R$ at a given θ) and compared to measurements where the same position is reached from the opposite side of the walls and so the arrangement crosses the centre, denoted with open symbols (i.e. the extension and frame penetrate a length $D - x > R$ at θ+180°). A clear radial profile is obtained in velocity and turbulence regardless of the use or not of an extension as long as the instrument does not cross the centre; otherwise a bias appears on the turbulence statistics, see bottom Fig. 13b. This phenomenon may be related to the

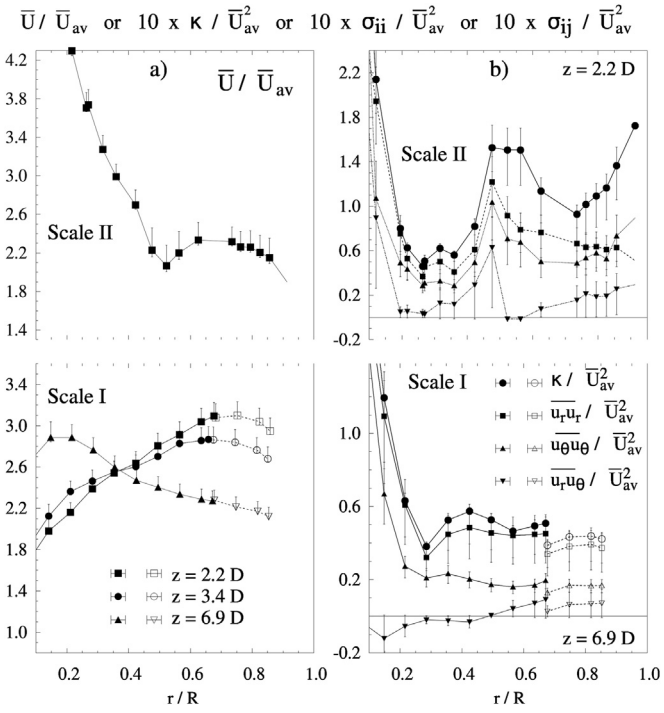

Fig. 13. Disruption to the vortex when using extensions. Open and solid symbols show respectively positions where the arrangement crosses or not the centre of the chamber. (a) $\bar{U}$ (b) κ, $\sigma_{\theta\theta}$, σ_{rr} and $\sigma_{r\theta}$. Scale I tower [32], Scale II tower [33].

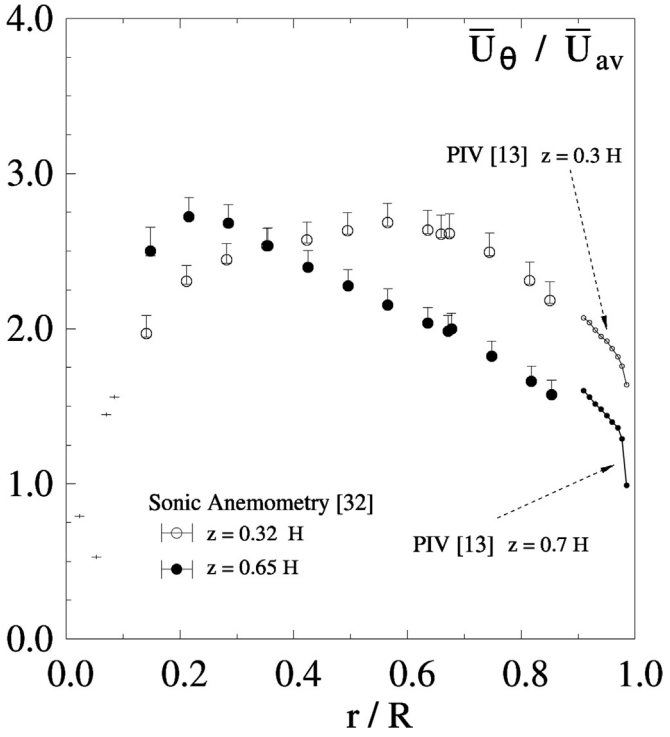

Fig. 14. Comparison against laser diagnostics methods, *PIV* [13].

precession of the vortex core, *PVC*, that is common in cyclones [65] and dryers [32,33]. It seems reasonable to believe that when the frame is allowed to destabilise the core it breaks the oscillation and disrupts the transport of turbulence in the horizontal plane. In this way, measurements collected when the arrangement crosses the centre provide a rough indication of velocity but should not be used to study variability.

6. Comparison to laser diagnostics methods in a tall-form dryer

The procedure and corrections described here have permitted studying the flow in dryers of very large scale [32,33]. Figs. 1b and 13 show some examples of the velocity fields in the towers named Scale I and II (Table 1). The vortex structure divided between the core and annular regions was found characteristic of a Rankine pattern in good agreement with literature [12,15,29]. Fig 14 includes a direct comparison between the tangential velocity U_θ collected at two axial levels with *PIV* and the corresponding sonic anemometry data [32] in comparable conditions. The agreement with *PIV* is evident and has important consequences. The work of Hassall [13] was the first to indicate that U_θ in a production unit was substantially lower than expected from *LDA* data collected in the same type of dryers at laboratory scale and with smooth walls [31]. Hassall could not describe the full structure of the flow nor analyse the reasons behind this because *PIV* could only reach a very limited area of the chamber. Access to the full geometry is now possible with anemometry and confirms the attenuation of the swirl. It also demonstrates that it is dependent on the roughness of the walls [32] and the type and coverage of the deposits formed in manufacture [33]. Velocity and turbulence data collected with sonic anemometers in a cleaned tower were successfully replicated with numerical models including roughness and friction [34]. This example and the agreement with *PIV* confirm the potential of the method and demonstrate the importance of having alternatives for full scale measurement. In addition, despite the limitations discussed, the measurement provided sufficient resolution to assess the impact of friction on the turbulence [33] and the frequency at which the core precesses [32].

7. Conclusions

This work introduces the use of sonic anemometry to study industrial confined swirling flows. It does not develop a new technique, but from an applied perspective looks into methods typical of meteorological, geomorphologic and aeronautics research to discuss the particularities of using these instruments in industrial devices. Further research would be required to extend the use of these instruments to other flow structures, particularly when significant velocity gradients develop in the measurement volume. In this paper, a useful guide has been given for engineers studying large cyclones or dryers, along with restrictions, appropriate signal corrections and an estimation of conservative range for the error. The main source is associated to the disruption caused by the instrument and has been linked to its geometry and orientation. The maximum range of measurement error when using a *HS*–50 under a turbulence level characteristic of swirl dryers and within recommended angles of attack, $\delta_{90th}<45°$ and $\lambda_{90th}>30°$, was found $<1-4\%$ in $\bar{U}$, $<1-3°$ in direction and $<7-31\%$ in κ, which is considered sufficient for this type of engineering applications where alternatives are very limited. Certain regions are excluded from the analysis (a) the core, $r<0.10R$, (b) the boundary layer, $r>0.98R$ and (c) regions nearby the contraction, $z>0.95H$. Other limitations arising from time averaging, calibration or the use of extensions have also been discussed.

In this way one could map very large geometries, far beyond the possibilities of optical techniques. Data are collected with simple modifications and in affordable way (~5*min* of shutdown time per location) but still retain a great level of detail. Considering that it should be compared with alternative techniques under the same operational challenges and conditions (i.e. volume,

operation regime and time), the method proposed represents a useful asset to improve the frequency of validation for large scale computational models in the particle technology industry. It is worth stressing that in the case of swirl dryers, it provided data in agreement with the only source of data available with *PIV* and allowed identification of features exclusively linked to production units such as friction, recirculation or periodicity.

Acknowledgments

VF was supported by an Engineering Doctorate Studentship sponsored by the Engineering and Physical Sciences Research Council (EPSRC) and Procter & Gamble in the Industrial Doctoral Centre in Formulation Engineering, School of Chemical Engineering, University of Birmingham (Grant no. EP/G036713/1).

Appendix A. Supporting information

Supplementary data associated with this article can be found in the online version at doi:10.1016/j.flowmeasinst.2016.06.017.

References

[1] J. Pruvost, J. Legrand, L. Legentialhomme, L. Doubliez, Particle image velocimetry investigation of the flow-field of a 3D turbulent anular swirling decaying flow induced by means of a tangential inlet, Exp. Fluids 29 (2000) 291–301.
[2] M.P. Escudier, J. Bornstein, N. Zehnder, Observations and LDA measurements of confined turbulent vortex flow, J. Fluid Mech. 98 (1) (1980) 49–63.
[3] M. Sommerfeld, H.H. Qiu, Detailed measurements in a swirling particulate two-phase flow by a phase-Doppler anemometer, Int. J. Heat. Fluid Flow. 12 (1) (1991) 20–28.
[4] I.V. Litvinov, S.I. Shtork, P.A. Kuibin, S.V. Alekseenko, K. Hanjalic, Experimental study and analytical reconstruction of precessing vortex in a tangential swirler, Int. J. Heat. Fluid Flow. 42 (2013) 251–264.
[5] O. Kitoh, Experimental study of turbulent swirling flow in a straight pipe, J. Fluid Mech. 225 (1991) 445–479.
[6] F. Chang, V.K. Dhir, Turbulent flow field in tangentially injected swirl flows in tubes, Int. J. Heat. Fluid Flow. 15 (5) (1994) 346–356.
[7] Z. Liu, J. Jinyu Jiao, Y. Zheng, W. Zhang, L. Jia, Investigation of turbulence characteristics in a gas cyclone by stereoscopic PIV, AICHE J. 52 (12) (2006) 4150–4160.
[8] L.X. Zhou, Y. Li, T. Chen, Y. Xu, Studies on the effect of swirl numbers on strongly swirling turbulent gas-particle flows using a phase-Doppler particle anemometer, Powder Technol. 112 (2000) 79–86.
[9] A.J. Hoekstra, J.J. Derksen, H.D.A. Van Den Akker, An experimental and numerical study of turbulent swirling flow in gas cyclones, Chem. Eng. Sci. 54 (1999) 2055–2065.
[10] H. Usui, Y. Sano, Y. Yanagimoto, Y. Yamasaki, Turbulent flow in a spray drying chamber, J. Chem. Eng. Jpn. 18 (3) (1985) 243–247.
[11] D.B. Southwell, T.A.G. Langrish, The effect of the swirl on the stability of spray dryers, TransIChemE 79 (2001) 222–234.
[12] I. Zbicinski, M. Piatkowski, Continuous and discrete phase behavior in countercurrent spray drying, Dry. Technol. 27 (12) (2009) 1353–1362.
[13] G. Hassal, Wall build up in spray driers EngD thesis, Chemical Engineering, University of Birmingham, Birmingham, UK, 2011.
[14] G. Fieg, G. Wozny, K. Buick, L. Jeromin, Estimation of the drying rate and moisture profiles in an industrial spray dryer by means of experimental investigations and a simulation study, Chem. Eng. Technol. 17 (1994) 235–241.
[15] S. Sharma, Spray dryer simulation and air flow pattern studies, The University of Aston, Birmingham. United Kingdom, 1990.
[16] H. Aouabed, J. Legrand, L. Legentialhomme, Wall visualization of swirling decaying flow using a dot-paint method, Exp. Fluids 19 (1995) 43–50.
[17] P. Wawrzyniak, M. Podyma, I. Zbicinski, Z. Bartczak, J. Rabaeva, Modeling of air flow in an industrial counter-current spray drying tower, Dry. Technol. 30 (2012) 217–224.
[18] F.G. Kieviet, J. Van Raaij, P.P.E.A. De Moor, P.J.A.M. Kerkhof, Measurement and modelling of the air flow pattern in a pilot-plant spray dryer, Trans. IChemE 75 (1997) 312–328.
[19] D.E. Oakley, Scale-up of spray dryers with the air of computational fluid dynamics, Dry. Technol.: Int. J. 12 (1–2) (1994) 217–233.
[20] A. Avci, I. Karagoz, Effects of flow and geometrical parameters on the collection efficiency in cyclone separators, J. Aerosol Sci. 34 (2003) 937–955.
[21] D.E. Oakley, Spray Dryer Modeling in Theory and Practice, Drying Technology: An International, 2004.
[22] B. Zhao, Development of a dimensionless logistic model for predicting cyclone separation efficiency, Aerosol Sci. Technol. 44 (12) (2010) 1105–1112.
[23] J.J. Derksen, H.E.A. Van den Akker, Simulation of vortex core precession in a reverse-flow cyclone, AIChE J. 46 (7) (2000) 1317–1331.
[24] G.I. Pisarev, V. Gjerde, B.V. Balakin, A.C. Hoffmann, H.A. Dijkstra, W. Peng, Experimental and computational study of the "End of the Vortex" phenomenon in reverse-flow centrifugal separators, AiCHE J. 58 (5) (2012) 1371–1380, Journal, 22, 6:1371-1402.
[25] C.H. Kim, J.W. Lee, A new collection efficiency model for small cyclones considering the boundary-layer effect, J. Aerosol Sci. 32 (2001) 251–269.
[26] I.C. Kemp, D.E. Oakley, Modeling of particulate drying in theory and practice, Dry. Technol. 20 (9) (2002) 1699–1750.
[27] D.J.E. Harvie, T.A.G. Langrish, D.F. Fletcher, A computational fluid dynamics study of a tall-form spray dryer, Trans. IChemE 80 (2002) 163–175.
[28] M. Mezhericher, A. Levy, I. Borde, Spray drying modelling based on advanced droplet drying kinetics, Chem. Eng. Proc. 49 (2010) 1205–1213.
[29] D.J.E. Harvie, T.A.G. Langrish, D.F. Fletcher, Numerical simulations of the gas flow patterns within a tall form spray dryer, Trans. IChemE 79 (2001) 235–248.
[30] D.H. Huntington, The influence of the spray drying process on product properties, Dry. Technol. 22 (6) (2004) 1261–1287.
[31] A.E. Bayly, P. Jukes, M. Groombridge, C. McNally, Airflow Patterns in a Counter-Current Spray Drying Tower - Simulation and Measurement. International drying symposium Sao Paulo 22-25 B, 2004, 775–781.
[32] V. Francia, L. Martin, A.E. Bayly, M.J.H. Simmons, An experimental investigation of the swirling flow in a tall-form counter current spray dryer, Exp. Therm. Fluid Sci. 65 (2015) 52–64.
[33] V. Francia, L. Martin, A.E. Bayly, M.J.H. Simmons, Influence of wall friction on flow regimes and scale-up of counter-current swirl spray dryers, Chem. Eng. Sci. 134 (2015) 399–413.
[34] M. Ali, Numerical modelling of a counter-current spray drying tower, University of Leeds, Leeds. United Kingdom, 2015.
[35] W. Steenbergen, J. Voskamp, The rate of decay of swirl in turbulent pipe flow, Flow. Meas. Instrum. 9 (1998) 67–78.
[36] J.C. Kaimal, J.E. Gaynor, H.A. Zimmerman, G.A. Zimmerman, Minimizing flow distortion errors in a sonic anemometer, Bound.-Layer. Meteorol. 53 (1–2) (1990) 103–115.
[37] O. Probst, D. Cardenas, Review state of the art and trends in wind resource assessment, Energies 3 (2010) 1087–1141.
[38] P.G. Mestayer, P. Durand, P. Augustin, et al., The urban boundary-layer field campaign in Marseille (UBL/CLU-ESCOMPTE): Set-up and first results, Bound.-Layer. Meteorol. 114 (2005) 315–365.
[39] D.W.T. Jackson, J.H.M. Beyers, K. Lynch, J.A.G. Cooper, A.C.W. Baas, I. Delgado-Fernandez, Investigation of three-dimensional wind flow behaviour over coastal dune morphology under offshore winds using computational fluid dynamics (CFD) and ultrasonic anemometry, Earth Surf. Process. Landforms 36 (2011) 1113–1124.
[40] S. Cao, T. Tamura, N. Kikuchi, M. Saito, I. Nakayama, Y. Matsuzaki, Wind characteristics of a strong typhoon, J. Wind. Eng. Ind. Aerodyn. 97 (2009) 11–21.
[41] A. Druilhet, P. Durand, Experimental investigation of atmospheric boundary layer turbulence, Atmos. Res. 43 (1997) 345–388.
[42] E.L. Andreas, R.J. Hill, J.R. Gosz, D.I. Moore, W.D. Otto, A.D. Sarma, Statistics of surface layer turbulence over terrain with metrescale heterogeneity, Bound.-Layer. Meteorol. 86 (1998) 379–408.
[43] M. Katurji, A. Sturman, P. Zawar-Reza, An Investigation into ridge-top turbulence characteristics during neutral and weakly stable conditions: velocity spectra and isotropy, Bound.-Layer. Meteorol. 139 (2011) 143–160.
[44] S.P. Oncley, T. Foken, R. Vogt, et al., The Energy Balance Experiment EBEX-2000. Part I: overview and energy balance, Bound.-Layer. Meteorol. 123 (2007) 1–28.
[45] M. Mauder, S.P. Oncley, R. Vogt, et al., The energy balance experiment EBEX-2000. Part II: intercomparison of eddy-covariance sensors and post-field data processing methods, Bound.-Layer. Meteorol. 123 (2007) 29–54.
[46] I.J. Walker, P.A. Hesp, R.G.D. Davidson-Arnott, B.O. Bauer, L. Steven, S. L. Namikas, J. Ollerhead, Responses of three-dimensional flow to variations in the angle of incident wind and profile form of dunes, Greenwich Dunes, Prince Edward Island, Canada 2009, pp. 127–138.
[47] D.M.D. Hendriks, J. Dolman, M.K. Van der Molen, J.A. Van Huissteden, Compact and stable eddy covariance set-up for methane measurements using off-axis integrated cavity output spectroscopy, Atmos. Chem. Phys. 8 (2008) 431–443.
[48] M.L. Goulden, J.W. Munger, S.M. Fan, B.C. Daube, S.C. Wofsy, Measurements of carbon sequestration by long-term eddy covariance: Methods and a critical evaluation of accuracy, Glob. Chang. Biol. 2 (3) (1996) 169–182.
[49] M. Aubinet, A. Grelle, A. Ibrom, et al., Estimates of the annual net carbon and water exchange of forests: The EUROFLUX methodology, Adv. Ecol. Res. 30 (2000) 113–175.
[50] B.W. Berger, K.J. Davis, C. Yi, P.S. Bakwin, C.L. Zhao, Long-term carbon dioxide fluxes from a very tall tower in a Northern Forest: flux measurement methodology, J. Atmos. Ocean. Technol. 18 (2001) 529–542.
[51] Gill Instruments Ltd. HS-50 Horizontally Symmetrical ultrasonic research anemometer. User Manual, 2004.1199, PS–0032, 02.
[52] A. Cuerva, A. Sanchez-Andres, On sonic anemometer measurement theory, J. Wind. Eng. Ind. Aerodyn. 88 (2000) 25–55.
[53] A. Cuerva, A. Sanchez-Andres, J. Navarro, On multiple-path sonic anemometer

measurement theory, Exp. Fluids 34 (2003) 345–357.
[54] A. Wieser, F. Fiedler, U. Corsmeier, The Influence of the sensor design on wind measurements with sonic anemometer systems, J. Atmos. Ocean. Technol. 18 (2001) 1585–1608.
[55] Gash JHC, A.J. Dolman, Sonic anemometer (co)sine response and flux measurement I. The potential for (co)sine error to affect sonic anemometer-based flux measurements, Agric. For. Meteorol. 119 (2003) 195–207.
[56] M.K. Van der Molen, J.H.C. Gash, J.A. Elbers, Sonic anemometer (co)sine response and flux measurement II. The effect of introducing an angle of attack dependent calibration, Agric. For. Meteorol. 122 (2004) 95–109.
[57] I.J. Walker, Physical and logistical considerations of using ultrasonic anemometers in aeolian sediment transport research, Geomorphology 68 (2005) 57–76.
[58] J.M. Wilczak, S.P. Oncley, S.A. Stage, Sonic anemometer tilt correction algorithms, Bound.-Layer. Meteorol. 99 (2001) 127–150.
[59] T. Nakai, M.K. Van der Molen, J.H.C. Gash, Y. Kodama, Correction of sonic anemometer angle of attack errors, Agric. For. Meteorol. 136 (2006) 19–30.
[60] S. Franchini, A. Sanchez-Andres, A. Cuerva, Effect of the pulse trajectory on ultrasonic fluid velocity measurement, Exp. Fluids 43 (2007) 969–978.
[61] S. Franchini, A. Sanchez-Andres, A. Cuerva, Measurement of velocity in rotational flows using ultrasonic anemometry: the flowmeter, Exp. Fluids 42 (2007) 903–911.
[62] A. Cuerva, A. Sanchez-Andres, O. Lopez, Singularities and undefinitions in the calibration functions of sonic anemometers, J. Atmos. Ocean. Technol. 21 (2004) 1868–1875.
[63] U. Hogstrom, A.S. Smedman, Accuracy of sonic anemometers: laminar windtunnel calibrations compared to atmospheric in situ calibrations against a reference instrument, Bound.-Layer. Meteorol. 111 (2011) 33–54.
[64] T. Nakai, K. Shimoyama, Ultrasonic anemometer angle of attack errors under turbulent conditions, Agric. For. Meteorol. 162–163 (2011) 14–26.
[65] C. Cortes, A. Gil, Modeling the gas and particle flow inside cyclone separators, Prog. Energy Combust. Sci. 33 (2007) 409–452.